
# An Alternative Method of Measuring Area Specific Resistance of Chromia Scales Using Electrochemical Impedance Spectroscopy

OPEN ACCESS

# An Alternative Method of Measuring Area Specific Resistance of Chromia Scales Using Electrochemical Impedance Spectroscopy

*Journal of The Electrochemical Society*, 2023 **170** 031505

# An Alternative Method of Measuring Area Specific Resistance of Chromia Scales Using Electrochemical Impedance Spectroscopy

**Alberto Visibile,[1,z] Luca Gagliani,[1] Elisabet Ahlberg,[2] Jan-Erik Svensson,[1] and Jan Froitzheim[1]**

[1]*Chalmers University of Technology, Department of Chemistry and Chemical Engineering, 41296 Gothenburg, Sweden*
[2]*University of Gothenburg, Department of Chemistry, 41296 Gothenburg, Sweden*

A novel method that employs electrochemical impedance spectroscopy (EIS) is developed to characterize the oxide scale resistance and thickness of Crofer 22 APU after exposure at 800 °C in humidified air. Crofer 22 APU, is one of the most commonly used materials for solid oxide fuel cell (SOFC) interconnects, an application for which oxide scale resistance is of paramount importance. The kinetics of oxide growth were studied for up to 6,000 h using three different techniques: electron microscopy of cross-sections, gravimetry, and EIS capacitance measurements of the oxide scale. EIS was used to evaluate the scale thickness starting from the material capacitance, and the material resistance at high temperature was estimated using extrapolation of the impedance values at room temperature. The result obtained with this novel EIS method are comparable to those obtained using conventional techniques, and in addition, the new method is cheaper, faster, and more reliable. Moreover, it enables repetitive exposures of the same sample without altering the specimen properties.
 [DOI: 10.1149/1945-7111/acc13e]

Manuscript submitted November 5, 2022; revised manuscript received February 24, 2023. Published March 20, 2023.

Supplementary material for this article is available online

High-temperature oxidation of ferritic stainless steel leads to the formation of semiconductive oxides on the surface of the steel. In chromium-containing alloys, the main oxidation product is $Cr_2O_3$. This is considered to be a protective oxide, and its growth commonly follows a parabolic rate law.[1–3] When manganese is present in the steel, a Cr-Mn spinel is typically observed on top of the Cr oxide scale.[4–8] While the formation of a $Cr_2O_3$ scale is desirable, since it inhibits the oxidation of iron, a higher growth rate is detrimental from several points of view. Rapid consumption of Cr for scale formation entails rapid depletion of this element from the bulk alloy, thereby reducing the lifetime of the material.[1–3] Thus, ideally, a material should be able to form a slow-growing $Cr_2O_3$ scale and be able to sustain it for a long time. Moreover, for specific applications that require the electrical conductivity of the metal, e.g., solid oxide fuel cells (SOFC), the formation of a $Cr_2O_3$ scale has to be minimized in order to avoid an increase in electrical resistance.[9,10] $Cr_2O_3$ acts as a semiconductor at high temperatures, with conductivity in the range of 0.003–0.05 S $cm^{-1}$at 800 °C.[11–14] Particularly in the case of interconnects, where the ferritic stainless steels have to withstand high temperatures (600°–850 °C)[7,8,4,15] and exhibit good electrical conductivity, it is essential to keep the scale as thin and as conductive as possible.[7,11,16,17] Many attempts have been made to reduce the resistance of interconnects by increasing $Cr_2O_3$ conductance. Some groups have used doping to increase the charge transfer inside the scale,[18,19] while others have modified the alloy itself to reduce the value of the parabolic oxidation kinetic constant $k_p$.[20,21] In addition, coatings such as cerium (Ce), have been used to reduce the oxide growth rate and, thus, the $Cr_2O_3$ thickness, resulting in resistance values lower than those of uncoated samples.[22–24]

The material selected for this study, Crofer 22 APU, is a tailor-made alloy for SOFC interconnects that are simultaneously exposed to an oxidizing gas (on one side of the plate) and to a fuel, usually $H_2$ plus water vapor (on the other side of the plate). This alloy gives promising results in terms of the oxidation rate and scale resistivity after high-temperature exposure.[5,8,25] More information about Crofer 22 APU can be found elsewhere.[26]

To follow the growth kinetics of the oxide scale, the most commonly used methods involve high-precision scales and repeated measurement of the sample weight over time or microscopic evaluation of the scale thickness over time using sample cross-sections. Although it provides more information on scale structure and homogeneity, the second method is time-consuming and can be strongly influenced by the regions chosen for the cross-sections. Gravimetric analysis, which measures mass gain (MG) due to oxygen uptake, is by far the most often used technique.[1,27] The scale thickness obtained from the gravimetric data can be affected by the formation of different oxides, although it is useful to follow the oxidation kinetic behavior of the material.

The evaluation of the material resistance instead is performed with the Area Specific Resistance measurement (ASR), which uses a four-wires measurement setup at high temperatures, with technical variations from one study to another.[11,12,16,28–32] The presented ASR values are calculated from the imposed current ($I$), the recorded potential ($E$), and the sample area ($A$) using Eq. 1:

$$ASR = \frac{E \cdot A}{I} \qquad [1]$$

The ASR technique has both advantages and disadvantages. On the one hand, it is beneficial to measure the resistance value at the working temperature and to evaluate the activation energy of the resistance. On the other hand, the method often displays a counter-intuitive decrease of the ASR value with time after an initial fast increase in the resistance value. This phenomenon is usually attributed to an improved electrical contact resulting from the growth of a $(Cr, Mn)_3O_4$ spinel between the top of the oxide layer and the contact itself.[31,33,34] Moreover, the ASR method is time-consuming (ramping up and down may require several hours to avoid scale spallation), and is expensive to run. It requires the use of a platinum paste and Pt sputtering to ensure good electrical contacts between the Pt electrodes and the oxide scale.[25] An additional limitation is that it is suitable only for samples of small dimensions because of common setup limitations. Most importantly, the samples cannot be used more than once because they are covered with Pt paste, which can affect the oxide scale microstructure.[9] Poor electrical contacts and difficult area determinations are also issues that must be taken into account at every measurement.

Electrochemical impedance spectroscopy (EIS) is a widely used method to quantify the quality of a coating on a metal substrate. The technique has been used extensively on inorganic layers, such as aluminum oxide on aluminum foil,[35–37] as well as on organic

[z]E-mail: visible@chalmers.se

coatings, such as paints.[38,39] EIS is a highly sensitive technique for assessing the coating's electrical and protective properties and structure (e.g., pores and channels, pit failure, the study of multiple layers, etc.).[40–43]

In the present study, the application of EIS at room temperature was used to measure the capacitance and resistance of the chromium oxide grown at 800 °C in humid air. From these measurements, it was possible to follow the material's oxidation kinetics and derive values for the scale thicknesses from the capacitance. Moreover, the room temperature resistance value measured with EIS could be related to the high-temperature ASR. The technique reduces the measuring time to less than 1 h, reduces the costs by eliminating the need for expensive Pt paste and electrodes, and increases the number of repeated exposures and measurements of the same sample, thereby minimizing the destructive impact of the technique. The method solves the area definition and electrical contact issues associated with ASR and returns, especially for thin scales, reliable values. Studying coated materials and pre-formed stack parts is also possible with EIS, and these will be evaluated in the future.

## Materials and Methods

***High-temperature exposures.***—For this study, 20 × 20 × 0.3 $mm^3$ coupons of Crofer 22 APU were used. The composition of the used batch is reported below in Table I using data from the supplier.

The as-received samples were ultrasonically cleaned twice in acetone and ethanol for 20 min, to remove any traces of grease or contamination. The dried samples were first weighed and then exposed isothermally in tubular furnaces in filtered pressurized air with a flow rate of 1,000 $ml \cdot min^{-1}$ at 800 °C for different periods of time. Several exposure times were selected, starting from a few minutes to 6,000 h. The samples were placed in the hottest zone of the furnace, where the temperature deviated by ±3 °C within 5 cm. All the exposures were performed in humidified air with 3% water vapor. The humidity level was controlled by a chilled mirror hygrometer (Michell-Optidew Vision). At least two exposures were performed for each exposure duration, to ensure reproducible results. After exposure, the samples were cooled in air, and the mass gains of all the samples were evaluated using a Mettler Toledo XP6 microbalance with a resolution of 0.1 $\mu$g.

***Electrochemical impedance spectroscopy (EIS).***—For EIS characterization, one side of the sample was manually ground with 1,200 grit paper using the Struers TegraPol-31 polishing machine, to generate an oxide-free electrical contact on the sample in the electrochemical cell. Only one side of the sample (the side with the oxide still present) was exposed to the electrolyte chosen for this experiment, 1 M $Na_2SO_4$ (the diameter of the exposed area was 1 $cm^2$). Other electrolytes could be used, as well as lower concentrations, but it is of mandatory importance that no chemical and electrochemical reaction with the electrolyte occurs in the experimental conditions. The stainless steel walls of the cell acted as the counter electrode, and an Ag/AgCl (3 M KCl reference electrode in a double-bridge filled with the cell electrolyte completed the electrode configuration. A schematic representation of the cell is presented in Fig. S1. EIS measurements were performed using the Princeton Applied Research (PAR) 4000 potentiostat/galvanostat in the range of 100 kHz to 10 mHz at open circuit potential (OCP) with an AC amplitude of 10 mV rms. Each sample was measured at least twice at two different locations on the surface. The average of the two values is presented. After impedance measurement, the sample was carefully washed and allowed to rest for at least 30 min in MilliQ® water to remove any traces of salt, then washed in ethanol and dried. The entire measuring method required less than 30 min according to the range of frequencies selected.

***Area-specific resistance (ASR).***—After mass gain measurements, selected samples were instead prepared for ASR measurement. As reported previously,[9–11,21,25,28,44] Pt is widely used as a contact material. In particular, in our procedure for ASR measurements, the samples were prepared by sputtering a defined area of 1 $cm^2$ with a thin layer of Pt, followed by painting with the Pt paste Metalor® 6926. Sintering of the Pt paint was achieved in a two-step process: a drying step for 10 min at 150 °C; and a sintering step for 1 h at 800 °C (the exposure temperature) in laboratory air.[11] The short sintering process time is not expected to change the ASR results for oxides exposed for much longer times. Considering the parabolic oxide growth, the effect of sintering can be also considered negligible. More caution must be applied for samples exposed for very short time. Hence these were not used when measuring ASR. More details of this procedure can be found in a previous publication.[9] The ASR values were then measured according to the 4-wires method in DC mode using the NorECs Probostat® (Norway) and a Keithley 2400 source meter.[45] The applied current was set to 100 $mA \cdot cm^{-2}$, and the ASR values were measured directly at the exposure temperature and during the cooling phase, to verify the semiconductive behavior. Considering the slow ramping up and reduction of the temperature (1 $C \cdot min^{-1}$), to avoid spallation of the oxide, the whole procedure required more than 20 h, limiting the number of samples that could be measured in a single day.

***Microscopy.***—Cross-sections were prepared by cutting the samples in half with an oil-free low-speed saw, followed by Leica TIC3X Broad Ion Beam (BIB) milling (3 mA, 8 kV, 5 h). This preparation method minimizes the mechanical load on the sample and thereby avoids the formation of cracks in the oxide scale.[46] SEM analysis was performed with a ZEISS Ultra 55 FEG scanning electron microscope in SE mode.

## Results and Discussion

To evaluate the electrolyte's effect and the rinsing procedure's performance, a series of mass gain measurements was performed on three different sets of samples. The first pair of samples was discontinuously exposed for 3 weeks and removed once a week for mass gain evaluation (samples D1 and D2) without any contact with the electrolyte. The second pair of samples was discontinuously exposed for 3 weeks. Every week, the samples were immersed for 30 min in the $Na_2SO_4$ solution to simulate the EIS measurement, rinsed with water and ethanol, and dried (samples E1 and E2). Mass gains were measured after every week of exposure. The third sample pair was exposed continuously for 3 weeks under the same conditions (samples C1 and C2). Figure 1 shows the mass gains of the different samples. No significant variations were observed for any of the samples. This means that neither the discontinuous exposure nor the immersion in $Na_2SO_4$ affected the scale growth kinetic, confirming the quality of the rinsing procedure.

The obtained values agree with the previously recorded results for the gravimetric analysis of Crofer 22 APU at the same temperature. Our finding of 0.42 $mg \cdot cm^{-2}$ recorded after 500 h of exposure is very similar to the value extrapolated from the value reported by Molin et al.[47] (around 0.4 $mg \cdot cm^{-2}$) and the value (0.36 $mg \cdot cm^{-2}$) found by Reddy et al.[48] after 500 h of exposure at the same temperature.

**Table I. Chemical composition of the used batch (data provided by the supplier).**

| Alloy | Fe | Cr | Mn | Si | Ti | C | Al | La |
|---|---|---|---|---|---|---|---|---|
| Crofer 22APU | Bal. | 22.74 | 0.45 | 0.02 | 0.06 | 0.002 | 0.01 | 0.11 |

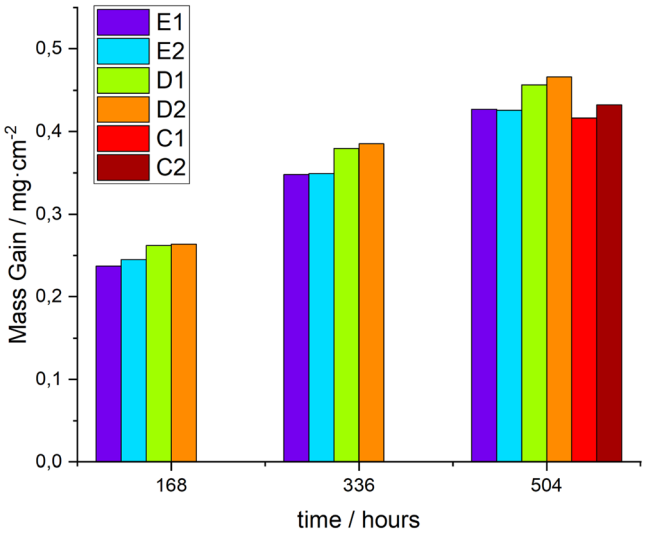


**Figure 1.** Mass gains in $mg{\cdot}cm^{-2}$ of the different samples of Crofer 22 APU exposed at 800 °C for 3 weeks. Samples labeled *E* were exposed discontinuously and immersed in the electrolyte once a week (blue and light-blue bars), while the samples labeled *D* were exposed discontinuously without any dipping into the electrolyte (green and orange bars), and the samples designated as *C* were continuously exposed for 3 weeks (red and brown bars).

Understanding the oxidation kinetics is of paramount importance for predicting the lifetimes of components operating at high temperatures and is related to the evolution of the oxide scale over time. The usual way to follow the growth kinetics of oxides is to measure oxygen intake through mass gains measurements with high-precision scales.

The expected mechanism for Crofer 22 APU under the applied conditions of flow, humidity, temperature and time is expected to be approximately parabolic.[47,49]

Parabolic oxidation can be described by Eq. 2:[1–3]

$$\Delta m^2 = k_p t + C \qquad [2]$$

where $\Delta m^2$ is the square mass change, $k_p$ is the parabolic rate constant, $t$ is the exposure time, and $C$ is an integration constant. Parabolic oxidation is seen for many metals and is commonly observed for Fe-Cr steels, and as described in the Wagner theory, the rate-determining step is the diffusion through the oxide scale. Consequently, the oxidation rate decreases with time as the thickness of the oxide scale increases.[50]

Figure 2 shows the SEM images of cross-sections of the oxide scale at different exposure times. The images show that the scale is composed, at all exposure times, of two different oxide scales: an outer one composed of (Cr,Mn)-spinel and an inner one of $Cr_2O_3$. As can be seen in Fig. 2, the ratios of the two layers change with time. The spinel phase grows rapidly in the earlier oxidation stages (from a few minutes to 1 week) and thereafter assumes a relatively stable thickness. Thus, the fraction of the $Cr_2O_3$ scale increases with time following a parabolic behavior. Two distinct parabolic oxidation constants have been derived. It is speculated that the first one is dominated by spinel formation and the second one is attributed to $Cr_2O_3$ scale growth. The respective recorded oxidation rate constants, $k_p$, are $1.8{\cdot}10^{-6}$ and $9.0{\cdot}10^{-6}$ $mg^{-2}cm^{-4}s^{-1}$. The $\Delta m^2$ vs time plot can be found in Fig. S2 in the Supporting Information. According to Niewolak et al.,[51] spinel formation is relatively quick and requires less than 12 h to form a continuous layer. The formation of the spinel seems to hinder the $Cr_2O_3$ by consuming most of the oxygen in the initial stages. A similar behavior with two time constants has been described by Mikkola et al.[52] Beneath the metal-scale interface, an internal oxidation zone (IOZ) of titanium is present with a depth that increases with the exposure time as oxygen penetration into the alloy increases. The thin bright layer on top of the scale is gold sputtered after the exposure for sample preparation purposes.

The average scale thickness was calculated with ImageJ from the scale's area using a polygonal fit. The area was then divided by image length to obtain an average scale height, so that the fluctuations in scale thicknesses were minimized. The values for the total scale, the $Cr_2O_3$ layer (darker region), and the spinel layer (brighter region) thicknesses are listed in Table II. The $Cr_2O_3$ fraction is calculated as the percentage of $Cr_2O_3$ thickness with respect to the whole scale. The spinel layer grew very rapidly at the beginning of the exposure and reached an almost constant value after 3,500 h. $Cr_2O_3$ instead became the main oxide for exposure times longer than 3 weeks. It is clear that initially two-thirds of the oxide scale are composed of spinel, whereas as the oxidation proceeds the $Cr_2O_3$ scale grows thicker, accounting for 84% of the oxide scale after 6,000 h of exposure.

Scale growth kinetics can be followed by gravimetric analysis, as well as by measuring the capacitance of the oxide scale of the sample used as an electrode in the EIS measurements. Information on the scale thickness can be obtained from the value of the real capacitance, $C_{real}$, of the oxide itself, as in Eq. 3.

$$C_{real} = \frac{Z_{im}}{2\pi f\left((Z_{real} - R_{sol})^2 - (Z_{im})^2\right)} \qquad [3]$$

where $Z_{im}$ and $Z_{real}$ are the imaginary and the real parts of the impedance measurement, respectively. $R_{sol,}$ is the solution resistance, which can be obtained from the complex plane (Nyquist) plot as the first intercept on the $x$-axis.[53]

A comparison of the gravimetric data and the capacitance values obtained by EIS (Fig. 3A) shows the proportionality between oxide scale growth over time and the recorded capacitance. Similar kinetics can be observed in the work of Megel et al.,[32] in which the exposures were performed at similar temperatures. In contrast to the microscopic evaluation of oxide scale thickness, both mass gain and EIS give an average value of a larger area of the sample thickness. However, in gravimetric measurements always the entire sample is measured, while EIS allows the possibility to select a specific area of interest on the sample surface. This is particularly useful in case of uneven oxide scale growth or when some surface differences are noticed. The area of interest can be easily adjusted by

**Table II. Average scale thicknesses obtained from the areas of different images. $Cr_2O_3$ and $(Cr, Mn)_3O_4$ are identified according to the different contrast profiles of the two oxides in the SEM images (Fig. 2).**

| Time (h) | Total thickness ($\mu$m) | $Cr_2O_3$ ($\mu$m) | $(Mn,Cr)_3O_4$($\mu$m) | $Cr_2O_3$ fraction |
|---|---|---|---|---|
| 168 | 0.78 | 0.27 | 0.51 | 0.35 |
| 336 | 1.34 | 0.52 | 0.82 | 0.38 |
| 504 | 1.53 | 0.60 | 0.93 | 0.39 |
| 2,000 | 5.54 | 4.19 | 1.35 | 0.75 |
| 3,500 | 9.68 | 7.51 | 2.17 | 0.78 |
| 6,000 | 12.18 | 10.27 | 1.91 | 0.84 |

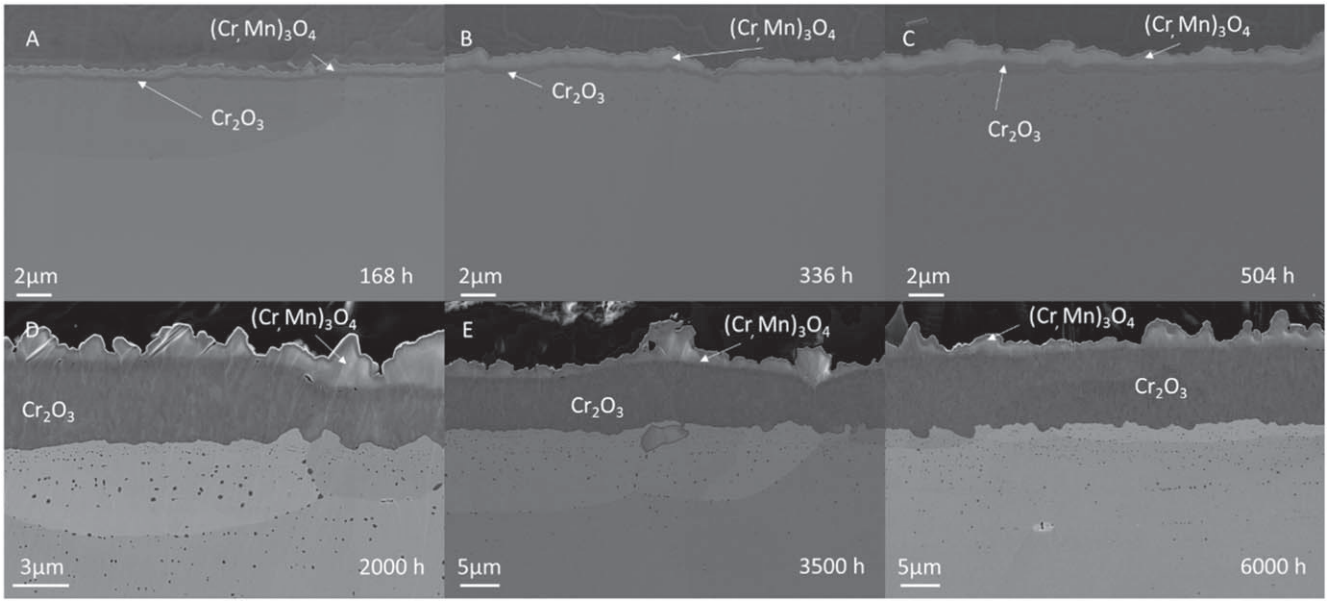


**Figure 2.** SEM cross-sections of Crofer 22 APU samples exposed for 168, 336, 504, 2,000, 3,500, and 6,000 h at 800 °C in 3% water vapor in humid air. Note the different magnifications of the images.

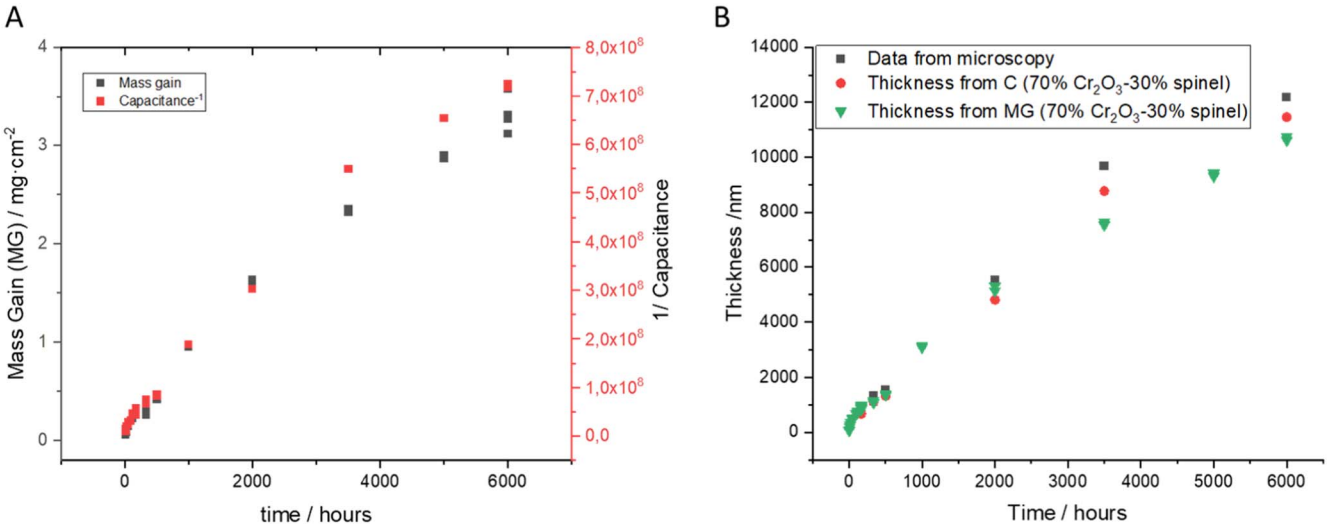


**Figure 3.** (A) Comparison of the mass gain values (in black) and capacitance$^{-1}$ (in red) assessed using impedance measurements. (B) Thickness (in nm) of the oxide calculated from: the cross-sections in Fig. 2 (black squares); the capacitance considering that the scale is composed of 70% $Cr_2O_3$ and 30% spinel (red circles); and the gravimetric analysis considering that the scale is composed of 70% $Cr_2O_3$ and 30% spinel (green triangles).

changing the hole in the electrochemical cell. In principle, any dimension can be used, but some limitation could arise with very small holes (<1 mm). Further analyses are needed to study the effect of the hole diameter and whether it contributes to variations in the results.

Figure 3(B) displays the evolution of the thickness of the oxide scale determined using three different methods. (I) Direct measurement using the SEM data presented in Fig. 2. (II) Using the mass gain and the density of the formed oxide to calculate the thickness of the oxide. A difficulty here is that the oxide scale of Crofer 22 APU is usually composed of chromium oxide and an outermost layer of Cr, Mn-spinel.[25,54,55] As presented in Table I, the ratio between the $Cr_2O_3$ scale thickness and the $(Cr,Mn)_3O_4$ changes with time. A trend for the variation of this ratio is reported in Table I using the values obtained from Fig. 2, showing how the relative importance of $Cr_2O_3$ increases with time. In Fig. 3B, this trend is neglected and 70% of the mass gain is attributed to the formation of $Cr_2O_3$ at all exposure times. The difference for the conversion between spinel and $Cr_2O_3$ is approximately 20%. (III) From the capacitance of the oxide obtained from Eq. 3, it is also possible to evaluate the oxide thickness using Eq. 4:

$$thickness = \frac{Area \cdot \varepsilon_0 \cdot \varepsilon_{oxide}}{C_{real}} \quad [4]$$

where $\varepsilon_0$ and $\varepsilon_{oxide}$ are the dielectric constants of a vacuum and the oxide layer, respectively.

Again it is assumed that the scale comprises 70% $Cr_2O_3$ and 30% $(Cr,Mn)_3O_4$. In the initial oxidation stage, this is an overestimation of the importance of $Cr_2O_3$ and a slight underestimation of the importance of $Cr_2O_3$ for longer exposure times. There is good agreement between these sets of data and the thickness observed by microscopy. The data on capacitance are obtained from an area of 1 cm$^2$, while the value from derived the cross-sections comes from a more limited section of the material, which may explain the slight differences.

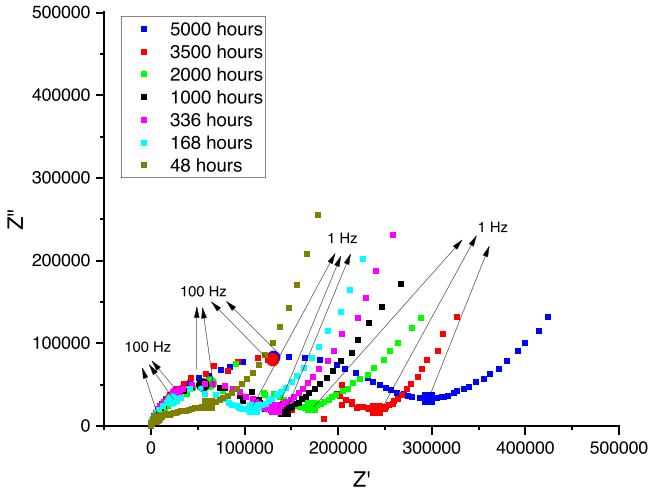


**Figure 4.** Impedance Nyquist plots of Crofer 22 APU samples exposed in humid air at 800 °C for different exposure times. EIS was performed in the frequency range of 100 kHz to 10 mHz at OCP with an AC amplitude of 10 mV rms in 1 M $Na_2SO_4$. Reference electrode: Ag/AgCl in 3 M KCl. The big circles highlight the 100 Hz frequency while the bigger square dots are at 1 Hz frequency.

To derive empirically the values of $\varepsilon_{oxide}$ ($Cr_2O_3$ and spinel), we used Eq. 4 and the capacitance obtained by EIS. In this calculation, it is assumed that after 168 h the scale is entirely composed of spinel, and that after 6,000 h it contains only $Cr_2O_3$. The values obtained for $\varepsilon_{oxide}$ are 13.83 and 20.89 for pure $Cr_2O_3$ and pure spinel, respectively. The $Cr_2O_3$ values are in good agreement with the ones of 11,8–13.3 obtained by Fang et al.,[56] and the value of 10.3 used by Dube et al.[57] for pure $Cr_2O_3$ scales. No previous information from the literature on the $\varepsilon_{oxide}$ value for the spinel has been found.

An advantage of EIS is that it is possible to determine both the scale oxidation kinetics and resistance from the same measurement. Oxide scale resistance is a parameter of extreme importance, especially in relation to fuel cell interconnects, where the resistance of the oxide scale contributes directly to stack degradation. One of the main purposes of this novel method is to evaluate the electric resistance of an oxide scale grown at high temperature. Figure 4 shows a comparison of the Nyquist plots for seven samples exposed for different exposure times. As expected, the impedance value increases with time, mainly due to the $Cr_2O_3$ oxide layer growth. Although the outer scale of Crofer 22 APU under these conditions is also composed of (Cr, Mn)-spinel,[58] the main contributor to electrical resistance during a long exposure time is the chromium oxide.[11,29]

The data presented in the Nyquist plot in Fig. 4, can be represented by a relatively simple equivalent circuit, as depicted in Fig. 5.

The solution resistance can be determined by reading the real axis value at the high-frequency intercept. For the measurements presented here, $R_{sol}$ is usually in the range of 15–20 Ohms. The real axis value at the low-frequency intercept is instead the sum of the oxide and solution resistances. The Warburg element is introduced to model a cell in which polarization arises from a combination of kinetic and diffusion processes, probably due to diffusion into the scale's pores.

The main contribution to the sample's impedance is from one oxide, the $Cr_2O_3$. Although a Cr, Mn-spinel is present, as shown in Fig. 2, its contribution to the total Z is minimal, and since it is relevant only for short exposure times, it is not considered in the equivalent circuit. The charge transfer resistance increases with exposure time as the thickness of the overall scale increases following the previously described parabolic equation. From Fig. 4, it is evident that the increase in the term $R_{ct} + R_{sol}$ is not linear with the exposure time. Despite this, it was challenging to obtain a reliable and straightforward fitting for $R_{ct}$ alone, especially for shorter exposure times. For this reason, the value of $Z_{tot}$ was used to acquire information on the scale resistance. This was found to be the ideal value to compare with the standard ASR values, to quantify the resistance of the oxidized sample. To ensure that the evaluation of $Z_{tot}$ was reproducible, the first derivative of the Bode phase plot was used. The frequency with value closer to zero of the first derivative function was used to calculate the $Z_{tot}$ values (reported in Fig. 7) as a function of sample thickness (calculated with the capacitance method). As it was not possible to separate the contributions of the two oxides, the overall value is presented as the total resistance of the oxide scale.

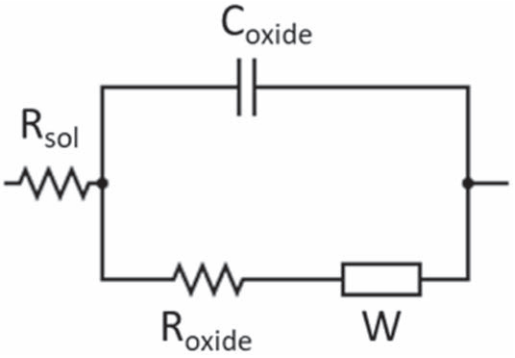


**Figure 5.** Simplified equivalent circuit for Crofer 22 APU with a scale of $Cr_2O_3$ in a solution of 1 M $Na_2SO_4$. $R_{sol}$ is the solution resistance, $R_{oxide}$ is the resistance for the charge transfer, $C_{oxide}$ is the capacitance of the oxide double layer, and W is the Warburg element for semi-infinite diffusion.

From a more traditional point-of-view, the resistance of the scale is proportional to its thickness according to Eq. 5:

$$R = \rho \frac{l}{A} \qquad [5]$$

where $\rho$ is the material resistivity, in this case, the $Cr_2O_3$ and $(Cr,Mn)_3O_4$ spinel, $l$ is the scale thickness, and $A$ is the area of the measured sample. As shown in Fig. 2, the oxide scales are relatively flat, i.e., have a constant thickness. The morphology of the oxide scale does not change over the studied timeframe, and the scale is dense and free of pores and cracks. However, the scale composition changes continuously (see Table I), as does the resistivity of the scale $\rho$.

Orazem and co-workers have developed a model for resistivity distribution in passive layers.[59–61] The most intriguing aspect of this model is the possibility to obtain information about the resistivity distribution within the oxide without assuming a specific equivalent circuit. For a perpendicular distribution, the resistivity of the oxide can be described by a power law:[60,61]

$$\frac{\rho}{\rho_\delta} = \xi^{-\gamma} \qquad [6]$$

where $\rho$ is the resistivity at a certain distance from the metal/oxide interface, $\rho_\delta$ is the resistivity at the oxide-solution interface, and $\xi$ is a dimensional parameter equal to $x/\delta$ where $\delta$ is the thickness of the oxide. The term $\gamma$ is a constant describing how steeply the resistivity varies and it depends on the parameter $\alpha$ in the constant phase element, $\gamma = 1/(1-\alpha)$. The resistivity at the metal/oxide interface also has a finite value, $\rho_0$, and the resistivity as a function of dimensional distance $\xi$ can be calculated according to:

$$\frac{\rho}{\rho_\delta} = \left(\frac{\rho_\delta}{\rho_0} + \left(1 - \frac{\rho_\delta}{\rho_0}\right)\xi^\gamma\right)^{-1} \qquad [7]$$

The values $\rho_\delta$ and $\rho_0$ are determined from the characteristic frequencies $f_\delta$ and $f_0$ according to:

$$\rho_\delta = \frac{1}{2\pi\varepsilon_r\varepsilon_0 f_\delta} \quad [8]$$

and

$$\rho_0 = \frac{1}{2\pi\varepsilon_r\varepsilon_0 f_0} \quad [9]$$

where $\varepsilon_r$ is the relative permittivity of the oxide and $\varepsilon_0$ is the vacuum permittivity. It is assumed that the dielectric constant does not change throughout the oxide. Even if that is not strictly true, the change in resistivity obtained from experimental data is much larger than any possible change in dielectric constant. In the present study, the dielectric constants used in the simulations were calculated from the oxide scale's known phase composition (see Table I and Fig. 2). The value at 1,000 h was obtained by extrapolation from the other points.

The characteristic frequency at the metal/oxide interface, $f_0$, is determined from the peak of the imaginary impedance (see Fig. S5). The resistance may be too high to allow a blocking oxide to be measured experimentally. The parameter $f_\delta$ is the characteristic frequency at the oxide/solution interface, and if the conductivity of the electrolyte is high, the resistivity at the oxide/electrolyte interface is not accessible, i.e., $f_\delta$ is outside the frequency range of the experiment. This applies to the present study, and the highest frequency was used to estimate a maximum value for the resistivity.[61]

With the model proposed by Hirschorn et al.,[59–61] the thickness of the layer needs to be determined using an independent method to describe the system. However, for passive layers, the impedance at high frequencies tends to approach ideal capacitive behavior, i.e., $\alpha$ approach 1, and a complex capacitance plot can be used to determine the layer thickness.[62] This method was applied here (see Fig. S4), and the total oxide thickness obtained was further used in the calculations of the resistivity distribution within the oxidized layer. Thus, the scale resistivity distribution changes with exposure time, as demonstrated in Fig. 6 using the oxide scale thickness from the capacitance and the $\rho$ value from Eq. 7.

Figure 6 shows the profiles of resistivity inside the oxide scales of different samples from the metal-oxide interface to the top of the scale. Samples with short exposure times start with a high resistivity value in the vicinity of the metal surface. This value rapidly decreases when moving away from the surface. In contrast, samples exposed for a long time show an initial region with high resistivity and a smoother decrease in resistivity within the scale. As shown in Fig. 2, the scale is mainly composed of the more-conductive spinel for short exposure times, and only a thin layer of $Cr_2O_3$ is present. This explains the rapid decreases in resistivity recorded for the samples exposed for 1 and 2 weeks. For longer exposure times, the inner part of the scale is made of more-resistant $Cr_2O_3$, while the more-conductive spinel makes up the outer part of the scale. The first plateau encountered is then related to $Cr_2O_3$ resistivity. The resistivity value decreases slowly, probably due to partial doping of the scale or possibly because the different $pO_2$ levels from one point to another affect the defect properties of the scale. The value at the oxide/electrolyte interface is the same, since it is given by the diffuse double layer in the electrolyte used. The shape of the curve is given by the dispersion factor $\alpha$ at high frequencies.

Interestingly, the starting value is different for the samples exposed for 1 and 2 weeks, indicating a more-resistive value than that seen for the longer exposures. The reason for this is presently unknown, and more experiments are needed to clarify this behavior.

Figure 7 shows a comparison of the standard ASR measurements performed at 800 °C with the 4-wires method using 100 mA of supplied current and EIS measurements performed at room temperature with the previously described parameters. Despite the differences in the absolute values (due to the semiconductive behavior of the material), the same trend of increasing resistance was recorded with time. This means that the method is a valid

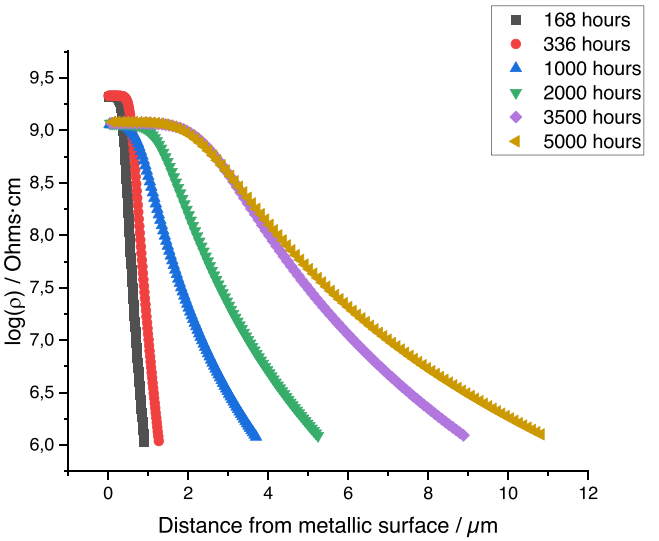


**Figure 6.** Resistivity distribution with distance from the metal surface of the different samples of Crofer 22 APU exposed at 800 °C for different times. EIS was performed in the frequency range of 100 kHz to 10 mHz at OCP with an AC amplitude of 10 mV rms in 1 M $Na_2SO_4$. Reference electrode: Ag/AgCl in 3 M KCl.

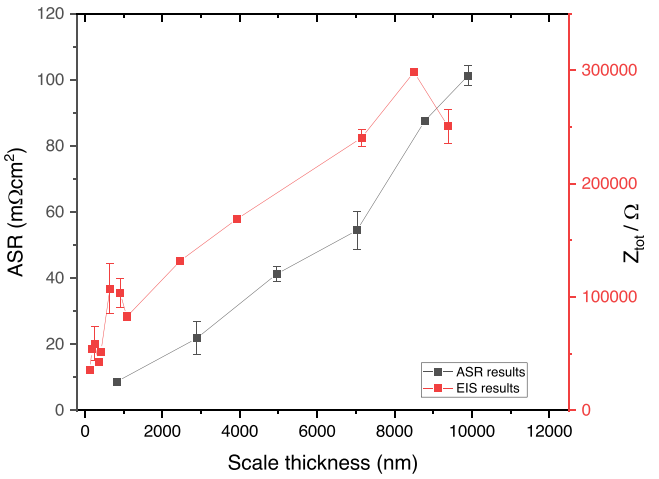


**Figure 7.** Comparison between the values recorded with EIS and those with standard ASR measurements at high temperature (800 °C) for Crofer 22 APU exposed at 800 °C for different times. EIS was performed in the frequency range of 100 kHz to 10 mHz at OCP with an AC amplitude of 10 mV rms in 1 M $Na_2SO_4$. Reference electrode: Ag/AgCl in 3 M KCl.

alternative that is able to provide similar data. The only value for which the ASR and EIS did not match was for the sample at 6,000 h. In this case, the $Cr_2O_3$ scale thickness exceeded 10 $\mu$m. The original material had a thickness of only 0.3 mm. Thus, excessive mechanical stress might have been applied to the sample during the surface contact preparation, creating cracks in the scale. These cracks may have formed preferential paths for the electrolyte, thereby yielding misleading Z values at the end of the measurements.

The values recorded with ASR are, in general, much smaller because the resistance (and thus the conductivity) of semiconducting materials changes with temperature, as described in Eq. 10:[13,14,63–66]

$$\sigma = \sigma_0 \, exp(-\Delta E/k_b T) \quad [10]$$

where $\sigma_0$ is a constant, $T$ is the temperature, $\Delta E$ is the activation energy, and $k_b$ is the Boltzmann constant. The values of $\sigma_0$ and $\Delta E$ can be obtained from a ln σ vs. 1/T plot using the values at the two

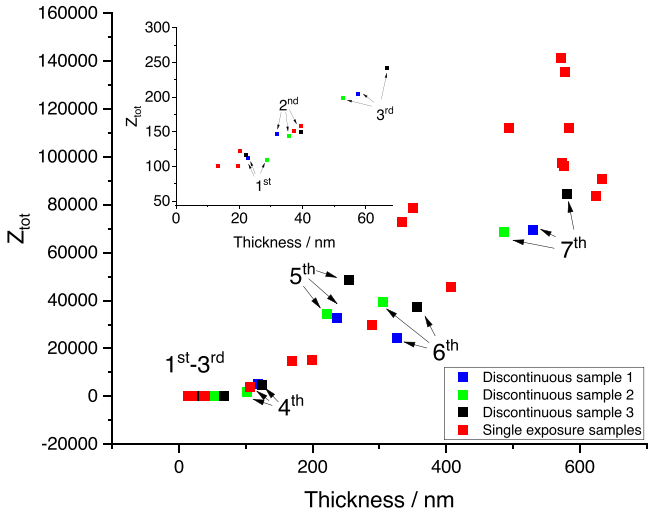


**Figure 8.** Impedance vs thickness comparison between one-shot samples (in red) and discontinuous samples (black, green, blue) of Crofer 22 APU exposed at 800 °C for different times. EIS was performed in the frequency range of 100 kHz to 10 mHz at OCP with an AC amplitude of 10 mV rms in 1 M $Na_2SO_4$. Reference electrode: Ag/AgCl in 3 M KCl.

different temperatures (25 °C and 800 °C).[63,64,67] From this simple equation, it is possible to convert the values obtained using EIS at room temperature and compare them, for example, with results in the literature obtained at high temperatures. The correlation may suffer a little from the scale composition variation with time. At the early stage of oxidation, the content of the slightly more-conductive spinel[68,69] exceeds that of the $Cr_2O_3$, and this may lead to minimal variation (circa 7 milli-Ohms) if the calibration line is obtained from a sample with a higher contribution from $Cr_2O_3$. As the composition becomes more constant for long exposure times, the correlation becomes more and more accurate. A cautious approach should be adopted, since minor scale changes in composition can arise if a different alloy is used. For this reason, a preliminary calibration with high-temperature ASR measurements is always recommended.

For our experiment, an activation energy of 0.56 eV was determined. This value agrees with the values recorded in the literature. Makhlouf et al.[65] reported an activation energy between 0.47 and 0.66 eV depending on the size of the $Cr_2O_3$ particles. Park et al.[14] calculated an average value of 0.55 eV, and Chu-Shen et al.[66] reported values in the range of 0.41–0.51 eV for measurements conducted above 500 °C. A similar range of values (0.51–0.65 eV) was described by Grolig et al.[16] for Co- and Co/Ce-coated samples, confirming $Cr_2O_3$ as the main contributor to the high resistivity of the sample. These results are intermediate to the value ranges found by Kofstad et al.[70,71] for pure $Cr_2O_3$: 1.8–1.6 eV at higher temperatures (1,000°–1,200 °C) and 0.20 eV at lower temperatures (900°–700 °C). This broad range is reflected in the different conductivities reported in the literature as depending on the oxygen partial pressure[14] and on doping with other alloying materials, which usually increases conductivity.[18,19]

One significant advantage of the presented method is that the $Z_{tot}$ value is usually relatively high and, thus, lies far from the detection limits of the instrument used. With ASR, especially for very thin scales, more-expensive instruments with high levels of accuracy need to be used, and sometimes the recorded value falls within the instrument error.

The possibility to perform repeated exposures on the same sample was tested. This is not possible with Pt-coated samples. With this novel method using EIS, it is possible to follow the behavior of an individual sample over an extended period of time if the cleaning procedure is carefully respected. Figure 8 shows the impedance $Z$ as a function of time for three different samples (blue, green, and black). This means that the samples have undergone the grinding-EIS-rinsing-exposure procedural series seven times. Those samples were compared with different specimens (red symbols) exposed just once for different amounts of time. From Fig. 8, it is clear that the trend is the same for up to seven measurements with this method. When more than seven measurements are made, the impedance recorded for the sample exposed discontinuously starts to decrease. This might be related to either stress-induced cracking of the sample oxide scale during the grinding procedure or slow doping of the scale with ions from the electrolyte. The use of thicker samples might be an advantage for future applications. These tests prove that EIS is less-destructive and more-flexible for the performance of multiple measurements on the same sample, as compared to conventional ASR characterization.

## Conclusions

This paper suggests an innovative method to evaluate metal oxide scale properties using a single measurement that is cheap, fast, reliable, and almost non-destructive. In particular, EIS measurements are useful for evaluating scale thickness and oxide growth kinetics, as an alternative to mass gain measurements. Moreover, with the same EIS measurement, it is possible in only 30 min to obtain the same information about the electrical resistance of the scale, as performed traditionally with the ASR method, which is slow, expensive, and sometimes involves complicated preparation. In addition, the proposed method allows re-exposure of the material several times after the resistance measurements, in contrast with the destructive ASR method. No influence of the electrolyte on the corrosion behavior is found when appropriate rinsing of the samples is performed. Nevertheless, too many thermal cycles combined with the measurement procedure give rise to a deviation, indicating the limit of the method. Further experiments with more complex alloys and, eventually, with coated steels will be performed in the future.

## ORCID

Alberto Visibile https://orcid.org/0000-0002-0198-9565
Luca Gagliani https://orcid.org/0000-0002-7393-9583
Elisabet Ahlberg https://orcid.org/0000-0002-4946-4979
Jan Froitzheim https://orcid.org/0000-0001-6339-6004

## References

1. N. Birks and G. H. Meier, *Introduction to the high temperature oxidation of metals* (Cambridge)(Cambridge University Press) (2006).
2. D. J. Young, *High temperature oxidation and corrosion of metals* (Amsterdam)(Elsevier) (2016).
3. C. A. C. Sequeira, *High Temperature Corrosion: Fundamentals and Engineering* (New York)(Wiley) (2019).
4. W. J. Quadakkers, J. Piron-Abellan, V. Shemet, and L. Singheiser, "Metallic interconnectors for solid oxide fuel cells—a review." *Mater. High Temp.*, **20**, 115 (2003).
5. W. Z. Zhu and S. C. Deevi, "Opportunity of metallic interconnects for solid oxide fuel cells: a status on contact resistance." *Mater. Res. Bull.*, **38**, 957 (2003).
6. Z. Yang, K. S. Weil, D. M. Paxton, and J. W. Stevenson, "Selection and evaluation of heat-resistant alloys for SOFC interconnect applications." *J. Electrochem. Soc. 150*, **9**, A1188 (2003).
7. J. Wu and X. Liu, "Recent development of SOFC metallic interconnect." *J. Mater. Sci. Technol.*, **26**, 293 (2010).
8. J. W. Fergus, "Metallic interconnects for solid oxide fuel cells." *Mater. Sci. Eng. A*, **397**, 271 (2005).
9. J. G. Grolig, J. Froitzheim, and J. E. Svensson, "Coated stainless steel 441 as interconnect material for solid oxide fuel cells: Oxidation performance and chromium evaporation." *J. Power Sources*, **248**, 1007 (2014).
10. K. Huang, P. Y. Hou, and J. B. Goodenough, "Characterization of iron-based alloy interconnects for reduced temperature solid oxide fuel cells." *Solid State Ionics*, **129**, 237 (2000).
11. C. Goebel, A. G. Fefekos, J. E. Svensson, and J. Froitzheim, "Does the conductivity of interconnect coatings matter for solid oxide fuel cell applications?" *J. Power Sources*, **383**, 110 (2018).
12. P. Huczkowski, N. Christiemsen, V. Shemet, L. Niewolak, J. Piron-Abellan, L. Singheiser, and W. J. Quadakkers, "Growth mechanisms and electrical conductivity of oxide scales on ferritic steels proposed as interconnect materials for SOFC's." *Fuel Cells.*, **6**, 93 (2006).
13. J. A. Crawford and R. W. Vest, "Electrical conductivity of single-crystal $Cr_2O_3$." *J. Appl. Phys.*, **35**, 2413 (1964).

14. J. H. Park and K. Natesan, "Electronic transport in thermally grown $Cr_2O_3$." *Oxid. Met.*, **33**, 31 (1990).
15. B. R. Sudireddy et al., "Development of robust metal-supported SOFCs and stack components in EU METSAPP consortium." *Fuel Cells.*, **17**, 508 (2017).
16. J. G. Grolig, J. Froitzheim, and J. E. Svensson, "Coated stainless steel 441 as interconnect material for solid oxide fuel cells: evolution of electrical properties." *J. Power Sources*, **284**, 321 (2015).
17. P. Piccardo, R. Amendola, S. Fontana, S. Chevalier, G. Caboches, and P. Gannon, "Interconnect materials for next-generation solid oxide fuel cells." *J. Appl. Electrochem.*, **39**, 545 (2009).
18. A. Holt and P. Kofstad, "Electrical conductivity and defect structure of Mg-doped $Cr_2O_3$." *Solid State Ionics*, **100**, 201 (1997).
19. A. Holt and P. Kofstad, "Electrical conductivity of $Cr_2O_3$ doped with $TiO_2$." *Solid State Ionics*, **117**, 21 (1999).
20. J. Froitzheim, G. H. Meier, L. Niewolak, P. J. Ennis, H. Hattendorf, L. Singheiser, and W. J. Quadakkers, "Development of high strength ferritic steel for interconnect application in SOFCs." *J. Power Sources*, **178**, 163 (2008).
21. V. Bongiorno, R. Spotorno, D. Paravidino, and P. Piccardo, "On the high-temperature oxidation and area specific resistance of new commercial ferritic stainless steels." *Metals (Basel).*, **11**, 1 (2021).
22. K. H. Tan, H. A. Rahman, and H. Taib, "Coating layer and influence of transition metal for ferritic stainless steel interconnector solid oxide fuel cell: a review." *Int. J. Hydrogen Energy*, **44**, 30591 (2019).
23. J. C. W. Mah, A. Muchtar, M. R. Somalu, and M. J. Ghazali, "Metallic interconnects for solid oxide fuel cell: a review on protective coating and deposition techniques." *Int. J. Hydrogen Energy*, **42**, 9219 (2017).
24. N. Shaigan, W. Qu, D. G. Ivey, and W. Chen, "A review of recent progress in coatings, surface modifications and alloy developments for solid oxide fuel cell ferritic stainless steel interconnects." *J. Power Sources*, **195**, 1529 (2010).
25. Y. Liu, "Performance evaluation of several commercial alloys in a reducing environment." *J. Power Sources*, **179**, 286 (2008).
26. VDM-Metals, VDM ® Crofer 22 AP, (2010), 10 http://vdm-metals.com/fileadmin/user_upload/Downloads/Data_Sheets/Datenblatt_VDM_Crofer_22_APU.pdf.
27. E. Mccafferty, *Introduction to Corrosion Science* (London)(Springer) (2004).
28. I. Antepara, I. Villarreal, L. M. Rodríguez-Martínez, N. Lecanda, U. Castro, and A. Laresgoiti, "Evaluation of ferritic steels for use as interconnects and porous metal supports in IT-SOFCs." *J. Power Sources*, **151**, 103 (2005).
29. K. Huang, P. Y. Hou, and J. B. Goodenough, "Reduced area specific resistance for iron-based metallic interconnects by surface oxide coatings." *Mater. Res. Bull.*, **36**, 81 (2001).
30. J. Li, W. Zhang, J. Yang, D. Yan, J. Pu, B. Chi, and L. Jian, "Oxidation behavior of metallic interconnect in solid oxide fuel cell stack." *J. Power Sources*, **353**, 195 (2017).
31. J. Tallgren, O. Himanen, M. Bianco, J. Mikkola, O. Thomann, M. Rautanen, J. Kiviaho, and J. Van Herle, "Method to measure area specific resistance and chromium migration simultaneously from solid oxide fuel cell interconnect materials." *Fuel Cells.*, **19**, 570 (2019).
32. S. Megel, E. Girdauskaite, V. Sauchuk, M. Kusnezoff, and A. Michaelis, "Area specific resistance of oxide scales grown on ferritic alloys for solid oxide fuel cell interconnects." *J. Power Sources*, **196**, 7136 (2011).
33. Z. Yang, J. S. Hardy, M. S. Walker, G. Xia, S. P. Simner, and J. W. Stevenson, "Structure and conductivity of thermally grown scales on ferritic Fe-Cr-Mn steel for SOFC interconnect applications." *J. Electrochem. Soc.*, **151**, A1825 (2004).
34. O. Thomann, M. Pihlatie, M. Rautanen, O. Himanen, J. Lagerbom, M. Mäkinen, T. Varis, T. Suhonen, and J. Kiviaho, "Development and application of HVOF sprayed spinel protective coating for SOFC interconnects." *J. Therm. Spray Technol.*, **22**, 631 (2013).
35. H. J. Oh, K. W. Jang, and C. S. Chi, "Impedance characteristics of oxide layers on aluminium." *Bull. Korean Chem. Soc.*, **20**, 1340 (1999).
36. J. A. González, V. López, A. Bautista, E. Otero, and X. R. Nóvoa, "Characterization of porous aluminium oxide films from a.c. impedance measurements." *J. Appl. Electrochem.*, **29**, 229 (1999).
37. J. Hitzig, K. Jüttner, W. J. Lorenz, and W. Paatsch, "AC-impedance measurements on porous aluminium oxide films." *Corros. Sci.*, **24**, 945 (1984).
38. F. Deflorian, L. Fedrizzi, S. Rossi, and P. L. Bonora, "Organic coating capacitance measurement by EIS: ideal and actual trends." *Electrochim. Acta*, **44**, 4243 (1999).
39. F. Deflorian and S. Rossi, "An EIS study of ion diffusion through organic coatings." *Electrochim. Acta*, **51**, 1736 (2006).
40. G. Wikmark, P. Rudling, B. Lehtinen, B. Hutchinson, A. Oscarsson, and E. Ahlberg, "The importance of oxide morphology for the oxidation rate of zirconium alloys." *ASTM Spec. Tech. Publ.*, **1295**, 55 (1996).
41. M. Oskarsson, E. Ahlberg, U. Andersson, and K. Pettersson, "Characterisation of pre-transition oxides on Zircaloys." *J. Nucl. Mater.*, **297**, 77 (2001).
42. M. Oskarsson, E. Ahlberg, and K. Pettersson, "Oxidation of Zircaloy-2 and Zircaloy-4 in water and lithiated water at 360 °C." *J. Nucl. Mater.*, **295**, 97 (2001).
43. S. V. Gnedenkov and S. L. Sinebryukhov, "Electrochemical impedance spectroscopy of oxide layers on the titanium surface." *Russ. J. Electrochem.*, **41**, 858 (2005).
44. I. Thaheem, D. W. Joh, T. Noh, and K. T. Lee, "Highly conductive and stable $Mn_{1.35}Co_{1.35}Cu_{0.2}Y_{0.1}O_4$ spinel protective coating on commercial ferritic stainless steels for intermediate-temperature solid oxide fuel cell interconnect applications." *Int. J. Hydrogen Energy*, **44**, 4293 (2019).
45. H. Falk-Windisch, *Improved Oxidation Resistance and Reduced Cr Vaporization from Thin-Film Coated Solid Oxide Fuel Cell Interconnects, PhD Thesis*, Chalmers University of Technology (2017).
46. R. Jiang, M. Li, Y. Yao, J. Guan, and H. Lu, "Application of BIB polishing technology in cross-section preparation of porous, layered and powder materials: a review." *Front. Mater. Sci.*, **13**, 107 (2019).
47. S. Molin, M. Chen, J. J. Bentzen, and P. V. Hendriksen, "High temperature oxidation of ferritic steels for solid oxide electrolysis stacks." *ECS Trans.*, **50**, 11 (2013).
48. M. J. Reddy, *Metallic materials in Solid Oxide Fuel Cells : Oxidation and chromium evaporation properties, Licentiate Thesis*, Chalmers University of Technology (2021).
49. S. Molin, M. Chen, and P. V. Hendriksen, "Oxidation study of coated Crofer 22 APU steel in dry oxygen." *J. Power Sources*, **251**, 488 (2014).
50. G. H. Meier, K. Jung, N. Mu, N. M. Yanar, F. S. Pettit, J. Pirón Abellán, T. Olszewski, L. Nieto Hierro, W. J. Quadakkers, and G. R. Holcomb, "Effect of alloy composition and exposure conditions on the selective oxidation behavior of ferritic Fe-Cr and Fe-Cr-X alloys." *Oxid. Met.*, **74**, 319 (2010).
51. L. Niewolak, D. J. Young, H. Hattendorf, L. Singheiser, and W. J. Quadakkers, "Mechanisms of oxide scale formation on ferritic interconnect steel in simulated low and high $pO_2$ service environments of solid oxide fuel cells." *Oxid. Met.*, **82**, 123 (2014).
52. J. Mikkola, K. Couturier, B. Talic, S. Frangini, N. Giacometti, N. Pelissier, B. R. Sudireddy, and O. Thomann, "Protective coatings for ferritic stainless steel interconnect materials in high temperature solid oxide electrolyser atmospheres." *Energies.*, **15**, 1168 (2022).
53. A. J. Bard and L. R. Faulkner, *Electrochemical Methods - Fundamentals and Applications* (New York)(Wiley) 2nd ed. (2001).
54. P. Gannon and P. White, "Oxidation of ferritic steels subjected to simulated SOFC interconnect environments." **16**, 53 (2009).
55. C. Folgner, V. Sauchuk, M. Kusnezoff, and A. Michaelis, "Influence of temperature and steam content on degradation of metallic interconnects in reducing atmosphere." *Ceram. Eng. Sci. Proc.*, **38**, 17 (2018).
56. P. H. Fang and W. S. Brower, "Dielectric constant of $Cr_20_3$ Crystals." *Phys. Rev.*, **126**, 1561 (1963).
57. D. C. Dube, D. Agrawal, S. Agrawal, and R. Roy, "High temperature dielectric study of $Cr_2O_3$ in microwave region." *Appl. Phys. Lett.*, **90**, 2006 (2007).
58. R. Sachitanand, M. Sattari, J. E. Svensson, and J. Froitzheim, "Evaluation of the oxidation and Cr evaporation properties of selected FeCr alloys used as SOFC interconnects." *Int. J. Hydrogen Energy*, **38**, 15328 (2013).
59. M. E. Orazem, B. Tribollet, V. Vivier, S. Marcelin, N. Pébère, A. L. Bunge, E. A. White, D. P. Riemer, I. Frateur, and M. Musiani, "Interpretation of dielectric properties for materials showing constant-phase-element (CPE) impedance response." *ECS Trans.*, **45**, 15 (2013).
60. B. Hirschorn, M. E. Orazem, B. Tribollet, V. Vivier, I. Frateur, and M. Musiani, "Constant-phase-element behavior caused by resistivity distributions in films." *J. Electrochem. Soc.*, **157**, C452 (2010).
61. B. Hirschorn, M. E. Orazem, B. Tribollet, V. Vivier, I. Frateur, and M. Musiani, "Constant-phase-element behavior caused by resistivity distributions in films." *J. Electrochem. Soc.*, **157**, C458 (2010).
62. M. Benoit, C. Bataillon, B. Gwinner, F. Miserque, M. E. Orazem, C. M. Sánchez-Sánchez, B. Tribollet, and V. Vivier, "Comparison of different methods for measuring the passive film thickness on metals." *Electrochim. Acta*, **201**, 340 (2016).
63. A. L. East, "An Arrhenius argument to explain electrical conductivity maxima versus temperature." *ECS Meet. Abstr.*, **50**(11), 3606 (2012).
64. D. P. Almond, A. R. West, and R. J. Grant, "Temperature dependence of the a.c. conductivity of Na/β-alumina." *Solid State Commun.*, **44**, 1277 (1982).
65. S. A. Makhlouf, Z. H. Bakr, H. Al-Attar, and M. S. Moustafa, "Structural, morphological and electrical properties of $Cr_2O_3$ nanoparticles." *Mater. Sci. Eng. B Solid-State Mater. Adv. Technol.*, **178**, 337 (2013).
66. C. S. Cheng, H. Gomi, and H. Sakata, "Electrical and optical properties of $Cr_2O_3$ films prepared by chemical vapour deposition." *Phys. Status Solidi Appl. Res.*, **155**, 417 (1996).
67. M. D. Julkarnain, J. Hossain, K. S. Sharif, and K. A. Khan, "Temperature effect on the electrical properties of chromium oxide ($Cr_2O_3$) thin films." *J. Optoelectron. Adv. Mater.*, **13**, 485 (2011).
68. Z. Lu, J. Zhu, E. Andrew Payzant, and M. P. Paranthaman, "Electrical conductivity of the manganese chromite spinel solid solution." *J. Am. Ceram. Soc.*, **88**, 1050 (2005).
69. N. Sakai, T. Horita, Y. P. Xiong, K. Yamaji, H. Kishimoto, M. E. Brito, H. Yokokawa, and T. Maruyama, "Structure and transport property of manganese-chromium-iron oxide as a main compound in oxide scales of alloy interconnects for SOFCs." *Solid State Ionics*, **176**, 681 (2005).
70. A. Holt and P. Kofstad, "Electrical conductivity and defect structure of $Cr_2O_3$. I. high temperatures (>∼1000 °C)." *Solid State Ionics*, **69**, 127 (1994).
71. P. Kofstad and K. P. Lillerud, "On high temperature oxidation of chromium: II. properties of and the oxidation mechanism of chromium." *J. Electrochem. Soc.*, **127**, 2410 (1980).